Rev. Roum. Sci. Techn.– Électrotechn. et Énerg.
Vol. **71**, *2*, pp. 235–240, Bucarest, 2026

GEOMETRY-DRIVEN MAGNETIC FIELD DECAY IN RECTANGULAR PERMANENT MAGNETS

ROBERT L. BERNAD[1], SANDOR I. BERNAD[2]

Keywords: Magnet geometry; Magnetic field decay; Magnetic field distribution; Magnetic field distribution; Spatial persistence.

The behavior of magnetic fields generated by permanent magnets is central to magnetic targeting applications, yet the influence of magnet geometry remains insufficiently characterized experimentally under controlled conditions. In this study, a systematic experimental framework was developed to isolate the effects of thickness and length in rectangular NdFeB magnets using a controlled 2×2 design and central-axis measurements. Field behavior was analyzed using complementary descriptors of local amplification, early axial decay, and spatial persistence, quantified by $A_h(z)$, D_r, and z_α, respectively. The results show that thickness primarily enhances near-field intensity, while length governs both spatial field persistence and early decay behavior. These effects are experimentally distinguishable, reflecting distinct geometry-dependent mechanisms. The study establishes a simple, experimentally validated framework for separating geometry-dependent contributions to magnetic field behavior, enabling consistent, physically interpretable comparisons of local amplification, early decay, and spatial persistence in targeting applications.

1. INTRODUCTION

Magnetic drug targeting (MDT) enables spatially controlled drug delivery by concentrating therapeutic agents at specific sites, with demonstrated potential in oncology and vascular interventions [1–3].

The effectiveness of MDT depends on magnetic forces proportional to $\nabla|B|^2$, making spatial field gradients critical for particle capture. However, rapid field decay limits penetration depth, particularly for deeper targets, constraining targeting efficiency under realistic conditions [4–8].

Previous studies have primarily focused on nanoparticle optimization and modeling approaches, often assuming predefined magnetic field distributions rather than explicitly addressing geometry-driven control of the magnetic field [9–17].

Despite the central role of the magnetic field source in determining targeting performance, the influence of magnet geometry on magnetic field behavior remains insufficiently characterized under controlled experimental conditions. In particular, the independent effects of fundamental geometric parameters, such as length and thickness, on field magnitude, spatial decay, and distribution patterns are not clearly established experimentally. More specifically, it remains unclear whether geometry-dependent contributions to local field amplification and spatial field decay can be isolated and interpreted independently under controlled conditions.

To address this gap, the present study introduces a controlled experimental framework designed to isolate the influence of magnet geometry on magnetic field behavior.

A structured 2×2 design space was investigated, in which magnet thickness and length were varied independently while all other parameters were kept constant. Magnetic field profiles were measured along the central axis under identical conditions, enabling direct comparison of geometry-dependent effects.

The analysis focuses on the experimental separation of local and global characteristics of the magnetic field, aiming to enable a controlled experimental assessment of how geometry influences magnetic field behavior.

While previous studies have predominantly relied on analytical or computational approaches to describe magnetic field behavior [4,10,13], the present work emphasizes direct experimental characterization under controlled conditions, providing a physically transparent, experimentally grounded, and directly interpretable basis for separating geometry-dependent contributions to magnetic field behavior.

2. MATERIALS AND METHODS

2.1 MAGNET CONFIGURATION

Four rectangular permanent magnets were selected to define a controlled geometric design space for the experimental analysis. All magnets were made of NdFeB (grade N35), ensuring consistent magnetic properties across the entire set. The width was kept constant at 20 mm, while two geometric parameters - length (L) and thickness (h) - were varied systematically.

The investigated configurations were 30×20×10 mm, 30×20×20 mm, 40×20×10 mm, and 40×20× 20 mm (L×W×h). This arrangement corresponds to a simple 2×2 design, where each parameter is varied independently at two levels. The 2×2 design was intentionally selected to isolate first-order geometric effects under controlled conditions, avoiding parameter coupling that would complicate interpretation. As a result, each pair of magnets differs by a single geometric dimension, allowing a direct comparison of its effect on the magnetic field.

The main characteristics of the investigated magnets are summarised in Table 1. A representative view of the magnets used in the experiments is shown in Fig. 1.

Table 1

Geometric and material properties of the permanent magnets investigated

Magnet ID	Length L [mm]	Width W [mm]	Thickness h [mm]	Material	Grade	Magnetization Direction
M1	30	20	10	NdFeB	N35	Through thickness
M2	30	20	20	NdFeB	N35	Through thickness
M3	40	20	10	NdFeB	N35	Through thickness
M4	40	20	20	NdFeB	N35	Through thickness

---

[1] Automation and Computers Faculty, University Politehnica Timisoara, Timisoara, Romania. E-mail: robert.bernad@student.upt.ro

[2] Romanian Academy Timisoara Branch, Timisoara, Romania. E-mail: sandor.bernad@upt.ro

DOI: 10.59277/RRST-EE.2026.2.11

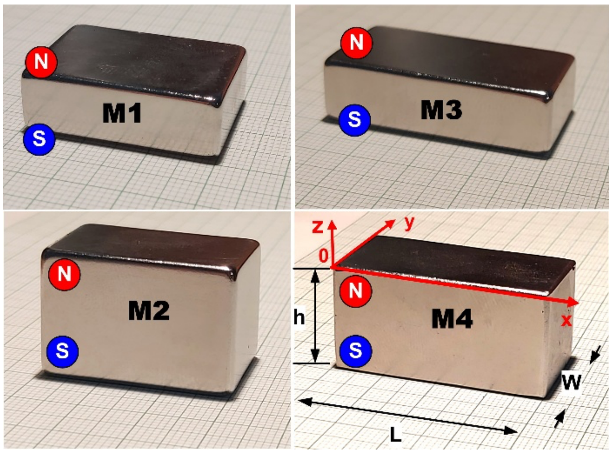

Fig. 1 – The image highlights the variation in length and thickness of the rectangular NdFeB permanent magnets, which defines the 2×2 geometric design space investigated in this study.

This configuration provides a controlled experimental framework in which magnet geometry is the only variable. This design enables direct experimental isolation of geometry-dependent effects, allowing changes in the measured magnetic field to be unambiguously attributed to variations in magnet dimensions, without additional sources of variability.

2.2 MEASUREMENT SETUP

Magnetic field measurements were performed using a digital teslameter (F.W. Bell 5080 Teslameter, Milwaukie, OR, USA) equipped with a Hall-effect probe suitable for static magnetic field characterization. The instrument provides a typical resolution of 0.01 mT and an accuracy of ±1% (±3 counts), which is sufficient to resolve millimeter-scale spatial variations in the magnetic field considered in this study. Measurements were performed exclusively along the magnet's central axis (z-axis), which is perpendicular to the magnet's surface and aligned with the magnetization direction.

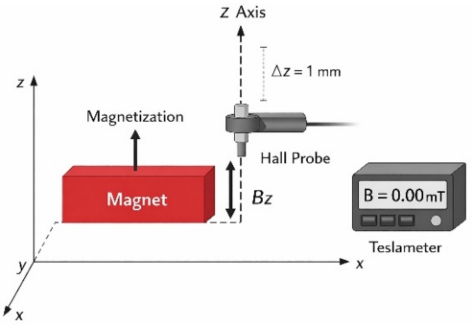

Fig. 2 – Schematic representation of the magnetic field measurement configuration. The diagram illustrates the measurement geometry, with the Hall probe positioned along the magnet's central axis and displaced incrementally along the z-direction. This configuration provides a well-defined, reproducible reference for evaluating spatial field decay while minimizing lateral geometric effects that could complicate interpretation. A minimum probe offset of approximately 0.35 mm from the magnet surface was maintained. The schematic representation emphasizes the essential geometric relationships of the measurement setup and facilitates reproducibility.

To ensure controlled positioning, the Hall probe was mounted on a mechanical translation stage, allowing precise displacement along the z-axis. Measurements were acquired with a spatial step of 1 mm, starting from near contact with the magnet surface and extending to distances where the magnetic field approached background levels. Due to the probe's finite size and protective housing, a minimum offset of approximately 0.35 mm from the magnet surface was maintained consistently across all measurements.

A schematic representation of the measurement configuration is shown in Fig. 2.

All measurements were performed under stable laboratory conditions, with the probe carefully aligned relative to the magnet surface. This ensured that the recorded variations in the magnetic field reflected the influence of magnet geometry rather than positioning errors or measurement artifacts, supporting the reliability and reproducibility of the experimental data. Measurement uncertainty is primarily determined by instrument accuracy and positioning precision, which were kept constant across all configurations.

2.3 MEASUREMENT PROTOCOL

For each magnet configuration, magnetic field measurements were performed along the central axis (z-axis), as defined in subsection 2.2. At each position, the axial component of the magnetic field (B_z) was recorded, providing a consistent reference for comparison across different geometries.

Measurements were acquired at discrete positions with a 1 mm spatial step, covering the region from near the magnet surface to distances where the field approached background levels. The acquisition sequence was kept identical for all magnets, ensuring direct comparability between datasets.

The recorded values were used as measured, without interpolation or smoothing. The data were organized as functions of distance from the magnet surface, enabling direct analysis of the field's spatial decay. These datasets form the basis for the comparative analysis presented in the Results section, ensuring consistent evaluation of magnetic field behavior across all configurations under identical acquisition conditions.

2.4 DATA PROCESSING AND NORMALIZATION

The measured magnetic field data were processed to enable a direct and consistent comparison between magnet configurations with different geometries. Since both the spatial coordinate and the magnetic field magnitude depend on magnet size, normalization was applied to remove scale-dependent effects and to reveal intrinsic geometry-driven trends.

The spatial coordinate was normalized with respect to the magnet length (L), defining a dimensionless distance:

$$z^* = \frac{z}{L}, \tag{1}$$

where z represents the measurement distance from the magnet surface.

The choice of magnet length as the normalisation parameter reflects its role as the characteristic spatial scale governing axial field decay in rectangular permanent magnets [18,19].

Similarly, the magnetic field was normalized relative to its maximum measured value for each configuration:

$$B^* = \frac{B(z)}{B_{\max}}, \tag{2}$$

where $B_{\max}$ corresponds to the maximum magnetic field measured along the central axis for a given magnet.

This normalization removes the influence of absolute field magnitude, which depends on both magnet volume and material properties, and enables direct comparison of the relative spatial evolution of the magnetic field across different geometries.

From a physical perspective, this approach is especially relevant for magnetic targeting applications [18]. While the absolute magnetic field determines the magnitude of the force acting on magnetic particles, the normalized field profile reflects how this force varies spatially relative to the magnet's size. This distinction is critical for understanding the balance between local capture and spatial reach, which defines the effectiveness of magnetic targeting systems.

2.5 DERIVED METRICS

To support the comparative analysis of magnetic field behavior, three simple comparative metrics were defined from the experimental data.

The first quantity was the thickness amplification factor, defined as:

$$A_h(z) = \frac{B_{\text{thick}}(z)}{B_{\text{thin}}(z)} \tag{3}$$

where $B_{\text{thick}}(z)$ and $B_{\text{thin}}(z)$ are the magnetic field values measured at the same axial position, z for two magnets with identical length and width, but different thicknesses.

The second quantity was the effective field range, defined as the axial distance $z_\alpha$at which the magnetic field decreases to a specified fraction $\alpha$of its maximum value. In this study, $z_\alpha$is explicitly defined as the first axial position satisfying the condition $B(z_\alpha)/B_{max} = \alpha$, ensuring a consistent and operational threshold-based characterization of spatial field decay,

$$\frac{B(z_\alpha)}{B_{\max}} = \alpha, \tag{4}$$

where $B_{\max}$ is the maximum measured magnetic field for a given magnet configuration.

The characteristic distances z_α were determined by linear interpolation between adjacent experimental points corresponding to $B(z_i) > \alpha B_{max}$ and $B(z_{i+1}) < \alpha B_{max}$. This definition ensures that the extracted $z_\alpha$values are directly comparable across all configurations and independent of absolute field magnitude.

The third quantity was defined as a field decay ratio, expressed as:

$$D_r = \frac{B(z_2)}{B(z_1)}, \tag{5}$$

where z_1 and z_2 represent two fixed axial positions selected within the measurement range.

In the present study, $z_1 = 1.35$ mm was chosen as a representative near-field reference, while $z_2 = 5.35$ mm corresponds to an early decay region along the central axis, consistent with the experimentally accessible measurement positions.

The selected positions correspond to experimentally stable and reproducible measurement points within the near-field and early decay regions, ensuring consistent comparison across configurations. The use of fixed reference points ensures direct comparability across all magnet configurations under identical measurement conditions.

Although the present analysis focuses on the magnetic flux density B(z), magnetic force generation in targeting applications is governed by the spatial gradient of the magnetic energy density, $\nabla|B|^2$. Therefore, variations in the measured field magnitude and spatial decay are expected to reflect corresponding changes in gradient magnitude and, consequently, in force generation capability. However, direct evaluation of magnetic field gradients and forces is beyond the scope of the present study and is not addressed here.

3. **RESULTS**

3.1 GLOBAL MAGNETIC FIELD BEHAVIOR

To provide an overall view of the magnetic field behavior across all investigated configurations, the magnetic flux density measured along the central axis is presented as a function of distance from the magnet surface (Fig. 3).

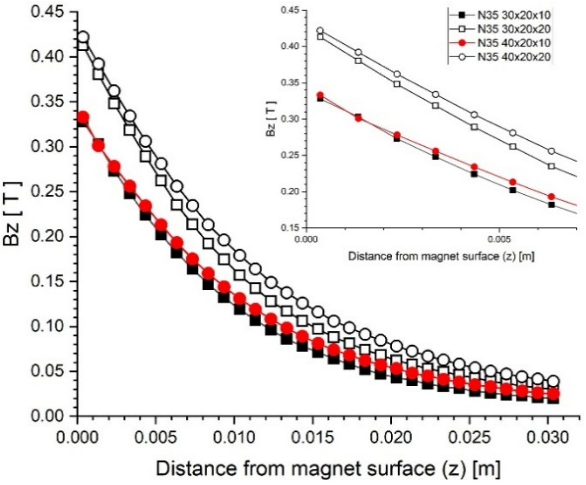

Fig. 3 – Magnetic flux density *B*(*z*) as a function of distance from the magnet surface for all investigated magnet configurations. Magnetic field profiles measured along the central axis for rectangular NdFeB magnets with different geometries (30×20×10 mm, 30×20×20 mm, 40×20×10 mm, and 40×20×20 mm). The curves allow direct comparison of field magnitude and spatial decay across configurations. Inset: zoom of the near-field region (0–5 mm) highlighting differences between configurations.

As shown in Fig. 3, all configurations exhibit a monotonic decrease in magnetic field magnitude with increasing distance from the magnet surface. Differences between the curves are evident both in the near-field region and at larger distances, indicating that the magnet geometry affects both the local field intensity and the spatial field decay.

3. THE EFFECT OF THICKNESS

To isolate the effect of magnet thickness, the magnetic field data were expressed using the amplification factor $A_h(z)$, defined as the ratio between the fields generated by magnets with identical length and width but different thickness (Fig. 4).

For both magnet lengths (Fig. 4), the amplification factor remains above unity across the entire measurement range, indicating a systematic increase in magnetic field magnitude with increasing thickness. The effect is most pronounced in the near-field region and decreases progressively with distance.

As the distance increases, the difference between the curves gradually decreases, although it remains detectable over the investigated range.

These results show that magnet thickness primarily affects local field amplification, with the strongest influence in the near-field region.

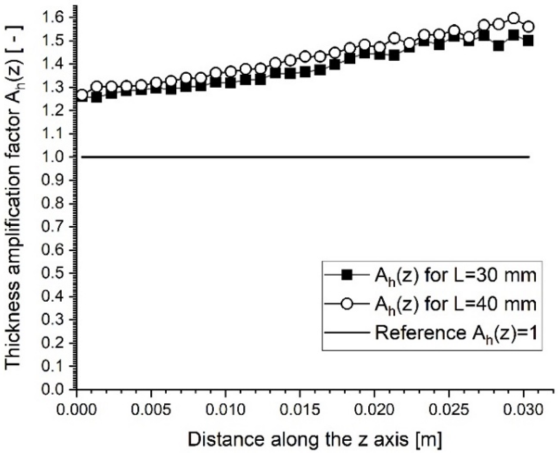

Fig. 4 – Thickness amplification factor $A_h(z)$ as a function of distance along the z direction. The amplification factor $A_h(z) = B_{\text{thick}}(z)/B_{\text{thin}}(z)$ is shown for magnet pairs with identical length (L = 30 mm and L = 40 mm) and thicknesses of 10 mm and 20 mm. The curves quantify the relative increase in magnetic field magnitude associated with increased thickness.

The field decay ratio D_r, evaluated between 1.35 mm and 5.35 mm, was used as a simple descriptor of early axial field decay. For magnets with the same length, the calculated D_r values increase only slightly with thickness, from 0.667 to 0.689 for $\mathrm{L} = 30$ mm and from 0.708 to 0.717 for $L = 40$ mm. These modest differences indicate that increasing thickness has a limited effect on early field decay, compared with its stronger influence on local field amplification, as reflected by the $A_h(z)$ profiles.

3.3 EFFECT OF LENGTH

To evaluate the influence of magnet length on the spatial persistence of the magnetic field, the effective field range was characterized using threshold-based metrics derived from the field decay profiles (Fig. 5).

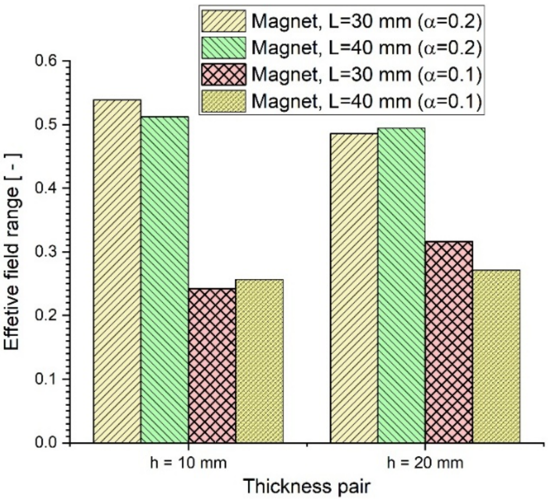

Fig. 5 – Effective field range metrics for different magnet lengths. Characteristic distances $z_{0.2}$ and $z_{0.1}$, defined as the positions where the magnetic field decreases to 20% and 10% of its maximum value, are shown for magnets with different lengths and identical thickness. These metrics quantify the spatial extent of the magnetic field.

In contrast to thickness, the effect of length is less pronounced near the magnet surface, where the magnetic field values remain relatively similar for both configurations (Fig. 5). However, as the distance increases, the difference between the curves becomes more evident, with longer magnets maintaining higher magnetic field values over a larger spatial range.

This behavior indicates that magnet length primarily determines the spatial extent of the magnetic field, *i.e.*, how far the field extends from the magnet surface. This effect is consistently captured by the threshold-based distances z_α, which provide a direct and quantitative measure of spatial field persistence. While the initial field magnitude is only moderately affected, the decay rate differs across configurations, leading to higher field values at larger distances for longer magnets.

3.4 EARLY FIELD DECAY ANALYSIS

Early axial field decay was characterized using the field decay ratio, D_r. This metric quantifies the relative reduction of the magnetic field between two experimentally consistent positions along the central axis, corresponding to the near-field region and the onset of field decay.

The metric was evaluated between 1.35 mm and 5.35 mm. The calculated values show a systematic dependence on magnet geometry. For magnets with identical length, increasing thickness results in only modest changes in D_r, from 0.667 to 0.689 for $\mathrm{L} = 30$ mm and from 0.708 to 0.717 for $\mathrm{L} = 40$ mm. This indicates that thickness has a limited influence on early axial field decay, consistent with the behavior observed for the amplification factor.

In contrast, increasing the magnet length leads to a more pronounced increase in D_r, from 0.667 to 0.708 for $\mathrm{h} = 10$mm and from 0.689 to 0.717 for $\mathrm{h} = 20$mm. This behavior reflects slower magnetic-field decay along the central axis in longer magnets, consistent with the extended spatial field range identified in Section 3.3.

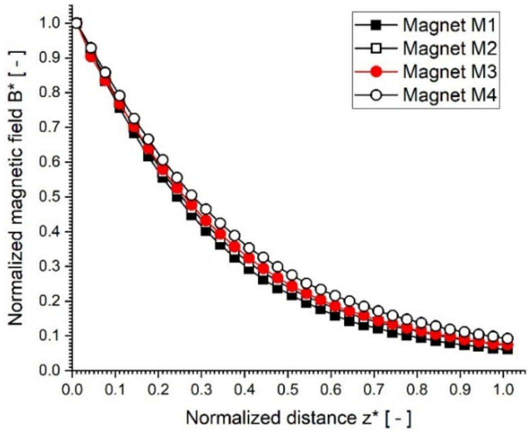

Fig. 6 – Normalised magnetic field $\boldsymbol{B}^*$ as a function of normalised distance z^*. Magnetic field profiles expressed as $B^* = B/B_{\max}$ and $z^* = z/L$ for all investigated configurations. This representation enables direct comparison of field decay independently of absolute magnet dimensions. The reduced variability highlights geometry-independent scaling behaviour, while residual deviations reflect thickness-dependent local effects.

The early decay behavior is further illustrated in Fig. 6, where the magnetic field is represented in normalized coordinates. When expressed as $B^*(z^*)$, the profiles corresponding to different magnet geometries exhibit reduced variability in the near-field region, while differences become more apparent at larger normalized distances. This indicates that the initial decay behavior is governed by similar scaling trends across configurations, whereas geometry-dependent effects become increasingly significant beyond the magnet's immediate vicinity. This representation indicates that part of the field decay behavior follows a geometry-independent scaling trend, while residual deviations reflect local thickness-dependent effects in the near-field region.

These results show that early field decay represents a distinct component of magnetic field behavior not captured by either local amplification or spatial persistence.

The combined use of these three complementary descriptors enables a more complete experimental characterization of the geometry-dependent magnetic-field behavior in rectangular permanent magnets.

4. **DISCUSSION**

This study demonstrates that the magnetic field behavior of rectangular permanent magnets can be quantitatively decomposed into three independent geometry-dependent components: local field amplification, early axial field decay, and spatial field persistence.

The analysis was restricted to the central axis to provide a well-defined, reproducible reference configuration, minimizing lateral geometric effects and enabling direct comparison between magnet geometries.

While this configuration does not capture full three-dimensional field variations, it provides a controlled reference for isolating geometry-dependent effects that would otherwise be difficult to separate experimentally.

The combined influence of magnet geometry on local field amplification, early axial field decay, and spatial field persistence is summarised in Table 2, which provides a comparative overview of all investigated configurations.

Table 2

Comparative summary of geometry-dependent magnetic field behavior. The parameters $z_{0.2}$ and $z_{0.1}$ represent threshold-based distances z_α, defined as the axial positions where the magnetic field decreases to 20% and 10% of its maximum value, respectively.

Configuration	$A_h(z_1)$	$A_h(z_2)$	D_r	$z_{0.2}$ [-]	$z_{0.1}$ [-]	Physical interpretation
30×20×10 mm	1.257	1.295	0.667	0.537	0.782	Baseline configuration, limited field persistence
30×20×20 mm	1.486	1.316	0.689	0.571	0.856	Increased local amplification, limited influence on early decay
40×20×10 mm	1.291	1.316	0.708	0.440	0.655	Reduced early decay and extended field persistence
40×20×20 mm	1.940	1.335	0.717	0.484	0.727	Combined local amplification and enhanced field persistence

The values reported in Table 2 confirm the trends observed in the experimental field profiles (Figs. 4 and 5) and provide a quantitative basis for comparing the influence of magnet geometry. The amplification factor $A_h(z)$ remains consistently above unity for all configurations and at both evaluated positions, indicating that increasing magnet thickness leads to a systematic enhancement of the magnetic field. The values at z_1 (near-field region) are higher than those at z_2, confirming that the effect of thickness is strongest close to the magnet surface and decreases progressively with distance. This behavior is consistent with the separation between near-field and intermediate-field regimes observed in Fig. 4. In contrast, the effective field range metrics $z_{0.2}$ and $z_{0.1}$ show a clear dependence on magnet length. For both thresholds, the values reported in Table 2 are consistently larger for the longer magnets (L = 40 mm), indicating that the magnetic field extends over a larger spatial range. This effect is directly observable in Fig. 5 and is now quantitatively captured through the characteristic distances z_α. These metrics are derived using a consistent threshold-based definition of z_α, enabling direct comparison of spatial persistence across configurations. The use of two thresholds ($\alpha = 0.2$ and $\alpha = 0.1$) further confirms that this behavior is robust and not dependent on a single arbitrary definition. The consistent increase in both $z_{0.2}$ and $z_{0.1}$ demonstrates that magnet length controls the spatial persistence of the magnetic field across multiple intensity levels. This separation provides a physically interpretable framework in which thickness controls local field amplification, while length governs both spatial persistence and early decay behavior, enabling independent tuning of these effects. The metric $A_h(z)$ captures local amplification effects associated with thickness, while z_α describing the spatial extent of the field governed by the magnet length. This three-part characterization is directly supported by both the experimental curves and the numerical values reported in Table 2.

The normalized representation indicates that magnetic field behavior reflects a combination of global scaling effects and local geometric variations. Compared with the existing literature, which often relies on modeling or predefined magnetic field distributions, the present study provides an experimental framework for isolating and quantifying geometry-dependent effects using simple descriptors [4,9–13]. More recent studies have emphasized the importance of controlled magnetic field gradients and spatial field engineering in biomedical applications, particularly for optimizing targeting efficiency and penetration depth [10-12,20]. In this context, the present study differs by providing direct experimental separation of these effects using simple, physically interpretable descriptors under controlled conditions.

From the perspective of magnetic field characterization, these results suggest a simple, physically interpretable framework in which magnet thickness is primarily associated with local field amplification, while magnet length governs both spatial persistence and early axial field decay. The combined use of $A_h(z)$, D_r, and z_α provides a practical and quantitative basis for describing these complementary aspects of magnetic field behavior.

The implications for magnetic drug targeting are direct. Although magnetic field gradients are not explicitly computed, the observed variations in field magnitude and spatial decay directly reflect the behavior of $\nabla|B|^2$ in the linear magnetization regime. Effective targeting requires both sufficient magnetic forces to capture particles and sufficient field penetration to reach the target region. The present results show that these requirements correspond to different geometric controls and can therefore be adjusted through distinct geometric contributions. Increasing thickness increases local field strength, while increasing magnet length extends the effective range of the magnetic field and slows axial field decay. This separation between local amplification, early field decay, and spatial persistence defines a more complete framework for understanding the trade-off between particle capture and penetration depth in magnetic targeting applications.

Overall, the results show that magnet geometry can be used to modulate local field amplification, early axial decay, and spatial field persistence through distinct geometric contributions, providing a direct basis for application-oriented magnetic field design. By combining experimental measurements with complementary quantitative descriptors, the present work provides a structured and experimentally grounded framework for understanding and comparing magnetic field distributions in practical applications. The analysis was restricted to the central axis and did not include direct evaluation of magnetic field gradients or dynamic flow conditions. These simplifications were adopted to isolate geometry-dependent effects and define directions for future work.

5. CONCLUSIONS

This study demonstrates that magnetic field behavior in rectangular permanent magnets can be quantitatively separated into three geometry-dependent components: local field amplification, early axial decay, and spatial persistence.

By introducing simple and experimentally grounded descriptors $A_h(z)$, D_r, and z_α, the analysis enables a consistent and physically interpretable comparison of these effects across different geometries. The results show that magnet thickness primarily controls local field amplification, while magnet length governs both spatial persistence and early decay behaviour, highlighting the possibility of independently tuning these contributions.

This framework provides a direct experimental basis for geometry-driven magnetic field design and supports the use of simple geometric parameters as practical control variables in applications requiring spatially controlled magnetic fields.

ACKNOWLEDGEMENT

This work was supported by the RA-TB/CFATR/LHC multiannual research program 2026–2030.

CREDIT AUTHORSHIP CONTRIBUTION STATEMENT

ROBERT BERNAD: Conceptualization, investigation, writing original draft.
SANDOR BERNAD: Methodology, validation, writing, review.

Received on 17 April 2026

REFERENCES

1. P.M. Price, W.E. Mahmoud, A.A. Al-Ghamdi, *Magnetic drug delivery: Where the field is going*, Frontiers in Chemistry, **6**, pp. 1–10 (2018).
2. L.H.A. Silva, F.F. Cruz, M.M. Morales, D.J. Weiss, P.R.M. Rocco, *Magnetic targeting as a strategy to enhance mesenchymal stromal cell therapy*, Stem Cell Research & Therapy, **8**, pp. 1–10 (2017).
3. M. Marcus, A. Smith, A. Maswadeh, Z. Shemesh, I. Zak, M. Motiei, H. Schori, S. Margel, A. Sharoni, O. Shefi, *Magnetic targeting of growth factors using iron oxide nanoparticles*, Nanomaterials, **8**, *9*, pp. 1–10 (2018).
4. E.J. Furlani, E.P. Furlani, *A model for predicting magnetic targeting of multifunctional particles in the microvasculature*, Journal of Magnetism and Magnetic Materials, **312**, *1*, pp. 187–193 (2007).
5. B. Chertok, B.A. Moffat, A.E. David, F. Yu, C. Bergemann, B.D. Ross, V.C. Yang, *Iron oxide nanoparticles as a drug delivery vehicle for MRI monitored magnetic targeting of brain tumors*, Biomaterials, **29**, *4*, pp. 487–496 (2008).
6. J. Owen, P. Rademeyer, D. Chung, Q Cheng, D. Holroyd, C. Coussios, P. Friend, Q.A. Pankhurst, E. Stride, *Magnetic targeting of microbubbles against physiologically relevant flow conditions*, Interface Focus, **5**, *5*, 20150001 (2015).
7. S.I. Bernad, E. Bernad, *Magnetic forces by permanent magnets to manipulate magnetoresponsive particles in drug-targeting applications*, Micromachines, **13**, pp. 1–10 (2022).
8. S.I. Bernad, E.S. Bernad, *Influence of PEG molecular weight on washout resistance and deposition efficiency of magnetoresponsive nanoclusters under pulsatile flow for magnetic drug targeting*, Pharmaceuticals, **18**, pp. 1–10 (2025).
9. C. Alexiou, W. Arnold, R.J. Klein, F.G. Parak, P. Hulin, C. Bergemann, W. Erhardt, S. Wagenpfeil, A.S. Lübe, *Locoregional cancer treatment with magnetic drug targeting*, Cancer Research, **60**, *23*, pp. 6641-6648 (2000).
10. A. Nacev, C. Beni, O. Bruno, B. Shapiro, *The behaviors of ferromagnetic nanoparticles in and around blood vessels under applied magnetic fields*, Journal of Magnetism and Magnetic Materials, **323**, 6, pp. 651–668 (2011).
11. E.A. Périgo, G. Hemery, O. Sandre, D. Ortega, E. Garaio, F. Plazaola, F.J. Teran, *Fundamentals and advances in magnetic hyperthermia*, Applied Physics Reviews, **2**, 4, pp. 1–54 (2015).
12. A.P. Khandhar, R.M. Ferguson, J.A. Simon, K.M. Krishnan, *Tailored magnetic nanoparticles for optimizing magnetic fluid hyperthermia*, J. Biomed Mater. Res. A., **100,** *3,* pp. 728–737 (2012).
13. B. Shapiro, S. Kulkarni, A. Nacev, A. Sarwar, P.Y. Stepanov, *Open challenges in magnetic drug targeting*, Wiley Interdisciplinary Reviews: Nanomedicine and Nanobiotechnology, **1**, *4*, pp. 446–457 (2012).
14. D.Ș. Nicolescu, A. Radulian, C.G. Sărăcin, M. Maricaru, *New solution of high force linear actuator with permanent magnets*, Rev. Roum. Sci. Techn. – Électrotechn. et Énerg., **69**, *2*, pp. 165–170 (2024).
15. C.M. Ciocăzanu, D.E. Nițescu, M. Morega, *Useful assumption for simplified numerical analysis of transcranial magnetic stimulation*, Rev. Roum. Sci. Techn. – Électrotechn. et Énerg., **70**, *3*, pp. 427–432 (2025).
16. A.A. Dobre, A.M. Ilie-Sandoiu, A.M. Morega, E. Gheorghiu, *Magnetic field control in an analytic platform for assessment of pathogenic bacteria*, Rev. Roum. Sci. Techn. – Électrotechn. et Énerg., **68**, *3*, pp. 317–322 (2023).
17. I. Stănică, R.G. Constantin, I. Lutan, A.A. Chitu, C.A. Boiangiu, *The impact of artificial intelligence on healthcare*, Rev. Roum. Sci. Techn. – Électrotechn. et Énerg., **70**, *3*, pp. 421–426 (2025).
18. E.P. Furlani, *Permanent Magnet and Electromechanical Devices: Chapter 4 Permanent Magnet Applications*, pp. 207–333, Academic Press (2001).
19. R. Engel-Herbert, T. Hesjedal, *Calculation of the magnetic stray field of a uniaxial magnetic domain*, Journal of Applied Physics, **97**, *7*, pp. 1–10 (2005).
20. S.I. Bernad, E.S. Bernad, *Magnetic drug targeting under pulsatile flow: A safety-constrained framework for deposition and retention stability*, Magnetochemistry, **12**, *40*, pp. 1–10 (2026).